

## Automated Identification Model of Ground-Glass Opacity in CT-Scan Image by COVID-19

Jufriadif Na'am<sup>a</sup>, Feriantano Sundang Pranata<sup>b,\*</sup>, Rahmat Hidayat<sup>c</sup>, Arrianda Mardhika Adif<sup>d</sup>, Ellyzarti<sup>e</sup>

<sup>a</sup>Universitas Putra Indonesia YPTK, Padang, 25221, Indonesia

<sup>b</sup>Universitas Muhammadiyah Jambi, Jambi, 36124, Indonesia

<sup>c</sup>Department of Information Technology, Politeknik Negeri Padang, 25164, Indonesia

<sup>d</sup>Universitas Indonesia, Jakarta, 16424, Indonesia

<sup>e</sup>Santa Maria Hospital, Pekanbaru, 28127, Indonesia

Corresponding author: \*feriantano@gmail.com

**Abstract**— Ground-Glass Opacity (GGO) is an object found in the thorax due to infection. This object interferes with the normal function of the thorax in breathing. The characteristic of GGO has slightly lighter turbidity compared to normal thorax tissue on radiological images, so it is very difficult to identify it precisely. This study aims to identify the GGO pattern and find the exact area of the CT-scan image of COVID-19 sufferers. The data tested were 34 images from 34 different patients. The image was taken using CT-Scan equipment with the tube model 46274891G1 axially. Each patient is taken one image with the reading position right above the chest using the file format Joint Photographic Experts Group (jpg). An automatic image processing model developed in this study uses several interrelated and continuous technical steps; Image Enhancement, Convert to Binary Image, Morphology Operation, Image Inverted, Active Contour Model, Image Addition, Convert Matrix to Grayscale, Image Filtering, Convert to Binary Image, Image Subtraction and Region Properties. The results of this study can identify GGO in all patient test images, where each patient has GGO. The smallest area of GGO was 3.9%, and the highest was 34.2% of the total thorax area. This level of comparison is greatly influenced by the severity of the COVID-19 virus patient. This area of GGO weakens the normal function of the thorax in the respiratory process of the patient. Thus, this research can be used as a model recommendation in identifying thorax damage due to COVID-19 very well in following up on more intensive treatment in the future.

**Keywords**— COVID-19; Ground-Glass Opacity (GGO); CT-scan; thorax; automated identification.

*Manuscript received 3 Dec. 2020; revised 31 Jan. 2021; accepted 9 Feb. 2021. Date of publication 30 Apr. 2021. IJASEIT is licensed under a Creative Commons Attribution-Share Alike 4.0 International License.*



### I. INTRODUCTION

China's Guangdong Province, the population of China, was infected with the Severe Acute Respiratory Syndrome (SARS) virus at the end of February 2003. This SARS virus is called SARS-CoV, which is a member of the beta sub-group Coronavirus [1]. At the end of 2019, a new virus emerged in Wuhan, China, killing hundreds and infecting thousands in just a few days. Then the World Health Organization (WHO) named this new virus as Coronavirus 2019 (2019-nCov). This virus affects respiratory distress and acute pneumonia [2]. In 2020, the International Committee on Taxonomy of Viruses (ICTV) stated that 2019-nCov is a Severe Acute Respiratory Syndrome Coronavirus-2 (SARS-CoV-2) or Coronavirus 2019 (Covid-19) [3]. COVID-19 is a family of Coronavirus from the beta group ( $\beta$ ) [4].

COVID-19 is a contagious virus that can spread very quickly and affect people globally. The virus is transmitted from an infected person to another through micron-sized droplets from the nose and/or mouth. Spread can occur through sneezing, coughing, and talking [5]. Common symptoms experienced by sufferers are body temperature above 38°C, coughing, and difficulty breathing. This virus affects the respiratory tract and creates a layer of lesions in the thorax that affects the function of the thorax itself. High severity can lead to pneumonia, acute respiratory syndrome, and death [6].

The test tool commonly used in detecting this virus is divided into two categories: anti-gene tests and antibody tests. The anti-gene tool is Polymerase Chain Reaction (PCR) [7]. The main drawback of this PCR is that it takes a long time, so it is inadequate with the number of sufferers [8]. Meanwhile, to identify thoracic damage, a scan or imaging

of the thorax must be carried out using a Computed Tomography CT-Scan [9], because there is a significant difference between images of healthy lungs and lungs of COVID-19 sufferers [10].

One indication of damage to the thorax due to COVID-19 is the appearance of a Ground-Glass Opacity (GGO) object [11]. The radiographic image shows that the GGO object is brighter than the normal chest tissue object because it does not contain air anymore [12]. Several studies published in PubMed, Embase (Elsevier), Google Scholar, and the World Health Organization (WHO) database contained 88% of sufferers who had GGO [13]. As many as 62 patients with pneumonia due to COVID-19 in Wuhan, China, 40.3% of the thorax contained GGO [14]. Of the 101 cases of COVID-19 sufferers aged 21-50 years in Hunan China, 86.1% of the thorax contained GGO [15]. Based on this research, there are physiological changes as an observation of the thorax organ for sufferers of COVID-19.

Radiologists in observing thorax images in COVID-19 sufferers are still subjective, so the analysis results are still biased because they are influenced by the observer's own experience [16]. Thus, understanding GGO is still in great demand and challenging due to the high variation in texture, size, and position accuracy presented in the CT-Scan image. GGO boundaries are still difficult to detect because of their low contrast and blurry appearance. For this reason, an automatic identification model is needed when using CT-Scan imaging of COVID-19 sufferers. This automatic identification will reduce manual involvement [17] so that image processing is needed.

Image processing is a solution that can be used in identifying GGO in COVID-19 sufferers. Several studies in processing X-Ray images of COVID-19 sufferers, including the use of the Convolutional Neural Network (CNN) Method with the Inception-Net technique based on Deep Learning, can identify negative or positive people with COVID-19 [18]. The Deep Neural Network technique of performing binary classification can determine positive or negative COVID-19 sufferers [19]. The ResNet18, ResNet50, SqueezeNet, and DenseNet-121 models on the CNN method can identify sufferers of COVID-19 [20]. The Transfer Learning Model on the CNN Method can automatically detect COVID-19 sufferers [21]. ResNet50, InceptionV3, and InceptionResNetV2 models in the Deep Learning Method can automatically detect COVID-19 sufferers [22]. The Pipeline for Advanced Contrast Enhancement (PACE) model by combining Fast and Adaptive Bidimensional Empirical Mode Decomposition (FABEMD) and Contrast Limited Adaptive Histogram Equalization (CLAHE) can detect lesions in COVID-19 sufferers [23].

Several studies in processing CT-Scan images, including the Harmony-search and Otsu method on thorax images, can detect COVID-19 sufferers [16]. Five models, namely AlexNet, VGG16, VGG19, GoogleNet, and ResNet50 on the CNN Method, can detect COVID-19 [24]. Deep learning methods based on Multi-Objective Differential Evolution (MODE) and CNN can classify positive and negative cases of COVID-19 sufferers [25]. The Pipeline for Advanced Contrast Enhancement (PACE) model by combining Fast and Adaptive Bidimensional Empirical Mode Decomposition (FABEMD) and Contrast Limited Adaptive

Histogram Equalization (CLAHE) can detect lesions in X-Ray images of COVID-19 sufferers [26]. So, in this study, a new method is proposed that can be used to automatically identify the patterns and extent of GGO on chest CT scans of COVID-19 sufferers. This research can be an alternative reference in conducting the initial screening process to make the right decisions in handling COVID-19 sufferers.

## II. MATERIALS AND METHOD

In identifying the GGO pattern on CT-Scan images of COVID-19 sufferers, several image processing processes are carried out. Each stage is interconnected and produces a new image that will be used as input for the next stage. The process stages in this research consist of Dataset, Image Enhancement, Convert to Binary Image, Morphology Operation, Image Inverted, Active Countour Model, Image Addition, Convert Matrix to Grayscale, Image Filtering, Convert to Binary Image, Image Subtraction and Region Properties. All stages of the process are carried out on a Personal Computer (PC) using the Matlab R2020b Software. The process stages are presented in Fig. 1.

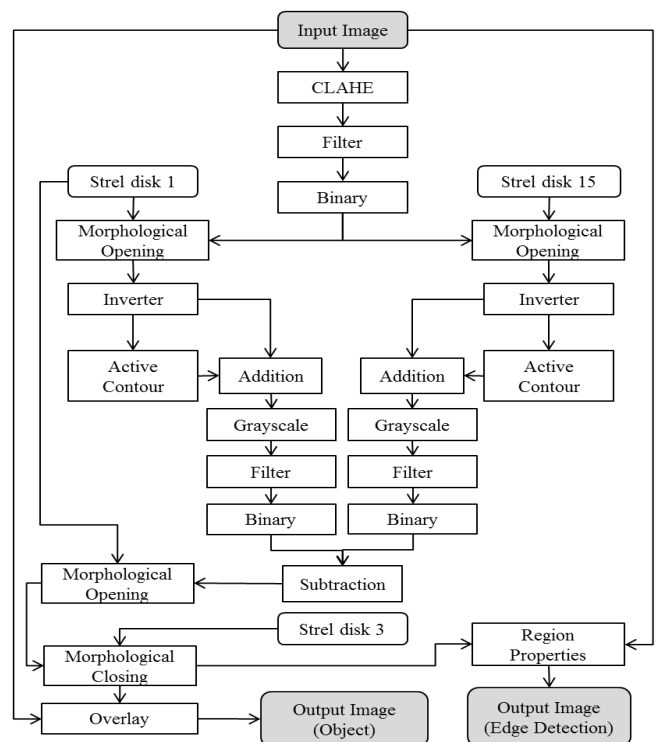


Fig. 1 Automatic Model Developed

### A. Input Image

The input image in this study is secondary data from patients who tested positive for COVID-19 sufferers based on the results of a swab test and doctor's expertise. The patient was scanned using a CT-Scan tool at the Radiology Section of the Santa Maria Hospital Pekanbaru. This hospital is located in Pekanbaru City, Riau, Indonesia. The number of data tested was 34 images from 34 different patients. The processed CT-Scan image is an image on the Axial slice acquired using a Computed Tomography (CT) tool with tube model 46274891G1 with tube serial number 117275BIB. Image format in the Joint Photographic Experts Group (jpg).

### B. Image Enhancement

At this stage, image contrast enhancement is needed in identifying objects in medical images [26]. The algorithm used in this model is Contrast Limited Adaptive Histogram Equalization (CLAHE). CLAHE is an algorithm used to correct low contrast problems in digital images, especially medical images. Especially in medical imaging, the results of the CLAHE algorithm are better than the Adaptive Histogram Equalization (AHE) and Histogram Equalization (HE) algorithm [27].

The CLAHE algorithm is assigned a clip limit which functions to cut certain values on the histogram. This value will remove the noise in the histogram, which will be smoothed, so it will produce a high contrast level [28]. The clip limit value is obtained from the Rayleigh distribution process with the equation presented in Formula (1) [29].

$$cl = cl_{\min} + \left[ 2(\alpha^2) \ln \left( \frac{1}{1 - DP(f)} \right) \right] \quad (1)$$

Where  $cl$  is the clip limit value,  $cl_{\min}$  is the minimum pixel value,  $DP(f)$  is the cumulative probability distribution which is a non-negative real scalar in determining the distribution parameter. Fig. 2 is an illustration of the CLAHE process carried out on the image [30].

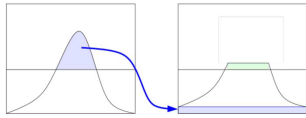


Fig. 2 CLAHE Illustration Process

### C. Convert to Binary Image

This stage converts from a grayscale image to a binary image using the thresholding algorithm. Binary image has two gray level values, namely black and white. The thresholding algorithm uses a threshold value that functions to separate the foreground/object from the background so that each area does not cover the other. Image pixels that have a value that exceeds or less than the threshold value, and then the pixels will be grouped into a predefined area [31]. Formula (2) is an equation used to convert grayscale to binary with the thresholding algorithm [32].

$$ag(x, y) = \begin{cases} 0, & \text{if } np(x, y) < NA \\ 1, & \text{if } np(x, y) \geq NA \end{cases} \quad (2)$$

$NA$  is the threshold value,  $np(x, y)$  is the pixel value, and  $ag(x, y)$  is the pixel value generated after the thresholding process. Fig. 3 is an illustration of the grayscale to the binary conversion process in the thresholding algorithm.

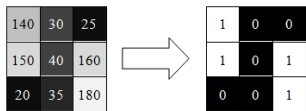


Fig. 3 Illustration of the binary image conversion process

### D. Morphology Operation

This stage performs a mathematical morphological process with the opening operation technique found in morphological surgery [33]. This operation requires an element structure (strel) to support the algorithm. The type

of string used is the disk type, whose matrix form is shown in Fig. 4.

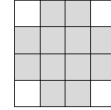


Fig. 4 Disc Structure Elements

The opening operation is an erosion operation followed by a dilation operation with the same string value. This operation is used to eliminate all pixels in an area that is too narrow and small in size and provide a smooth surface to the object. So that the erosion operation will remove the smaller area of the structural elements, and the larger area will be smoothed by the dilation operation [34]. The dilation equation is presented in Formula (3) [35].

$$CI \circ EP = (CI \ominus EP) \oplus EP \quad (3)$$

Where  $CI$  is the object of the test image,  $EP$  is a structural element,  $CI \circ EP$  is the result of the opening morphology process,  $CI \ominus EP$  is a process of erosion operations, and  $(CI \ominus EP) \oplus EP$  is a process of dilation operations.

### E. Image Inverted

This stage carries out the process of reversing the image's pixel value, which results in an image with a negative value. Each pixel value is modified by reducing the original intensity value to the maximum intensity value. The value of each pixel in this process is only 1 bit deep, so the pixel value only has two color intensity values, namely 0 (black) and 1 (white). This process shows that black and black pixel values replace white pixel values are replaced with white. The equation of the reverse process is presented in Formula (4) [36].

$$S(x, y) = L - 1 - R(x, y) \quad (4)$$

Where  $S(x, y)$  is the result of the reverse process,  $L$  is the maximum intensity value and  $R(x, y)$  is the original intensity value. Fig. 5 is an illustration of the inverted process carried out on the image.

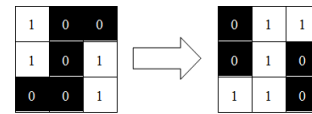


Fig. 5 Illustration of an inverted image process

### F. Active Contour Model

This stage is an Active Contour process model, where this process forms a closed curve to map the area of an object. The area of the curve can move broadly or narrowly. The active contour model uses the principle of energy minimizing which detects certain objects in the image [37]. In Active Contour Model, it will create an initial contour around the object, and the curve will shrink according to the pattern of the object [38] so that the curve only surrounds the object. An illustration of the Active Contour Model is shown in Fig. 6.

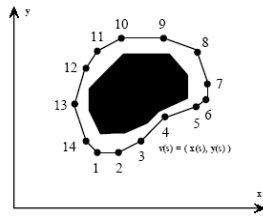


Fig. 6 Illustration of the active contour model process

Parameters used in Active Contour in determining coordinate curve points are presented in Formula (5) [39].

$$ac(s) = (k(s), l(s)) \quad (5)$$

Where  $k(s)$  and  $l(s)$  are the coordinates of  $k$  and  $l$  on the contour  $ac$  and  $s$ , which are the index normalization of the control point. The energy force function presented consists of two components, namely internal and external. The internal energy force has a function to make a compact curve (elastic force), and its boundaries are very sharp turns (bending force). The external energy force causes the curve to move only towards the object boundaries. The internal energy force as the sum of the elastic energy and flexibility energy is presented in Formula (6).

$$E_{int} = E_{elastic} + E_{bend} = \alpha(s) \left| \frac{dv}{ds} \right|^2 + \beta(s) \left| \frac{d^2v}{ds^2} \right|^2 \quad (6)$$

Where  $\alpha$  is the constant of the elasticity variable, and  $\beta$  is the constant of the curvature of the contour curve. Energy elasticity and flexibility are presented in Formula (7) and Formula (8). Meanwhile, the energy minimization is presented in Formula (9)

$$E_{elastic} = \int_s a(v(s) - v(s-1))^2 .ds \quad (7)$$

$$E_{bend} = \int_s \beta(v(s-1) - v(s) + v(s+1))^2 .ds \quad (8)$$

$$E_{snake}^* = \int_0^1 E_{snake}(v(s)) .ds = \int_0^1 \{E_{int}(v(s)) + E_{image}(v(s)) + E_{con}(v(s))\} .ds \quad (9)$$

Where  $E_{int}$  is the internal energy of the curve,  $E_{image}$  is the energy of the image, and  $E_{con}$  is the external energy.

### G. Image Addition

At this stage, 2 images that have the same matrix are added. This process aims to determine a pixel value that is only 0 in the same axis position, which will form the edge as black. The equation of this operation is presented in Formula (10) [40].

$$CO(x, y) = CI1(x, y) + CI2(x, y) \quad (10)$$

Where  $x$  is the pixel position value for rows,  $y$  for columns,  $CO(x, y)$  is the result of the addition process.  $CI1(x, y)$  is the added pixel value in the first image, and  $CI2(x, y)$  is the added pixel value in the second image. An illustration of the addition process is presented in Fig. 7.

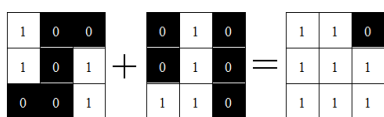


Fig. 7 Illustration of image addition process

### H. Convert Matrix to Grayscale Image

At this stage, image normalization is carried out by converting the matrix into a grayscale image. The process is carried out by scaling the matrix elements using a linear transformation, each pixel with the lowest value is converted to a value of 0, and the highest pixel value is converted to a value of 1. The results of this stage will produce an image with a pixel value of double-type data [41]. The equation used in this process is presented in Formula (11) [42].

$$GI = \frac{CY - CY_{min}}{CY_{max} - CY_{min}} \quad (11)$$

Where  $GI$  is the conversion value,  $CY$  is the pixel value,  $Y_{min}$  is the image minimum pixel value and  $Y_{max}$  is the image maximum pixel value.

### I. Image Filtering

At this stage, noise is removed from the image. The algorithm used is a non-linear filter, namely the Median Filter algorithm [43]. The process in this algorithm performs filtering of the position of the pixel value on all pixel values in the image. Pixel position will be shifted sequentially from smallest pixel value to largest value. After the position has been sorted from smallest to large value, then the pixel value is determined in the middle position (media). The median pixel value will be the pixel value at the center of the filter plane. The equation used is presented in Formula (12) [44].

$$mf(x, y) = median \sum_{(s,t) \in ks_{xy}} cg(s, t) \quad (12)$$

Where  $mf(x, y)$  is the result of the median filter,  $ks_{xy}$  is the coordinate of the filter and  $cg(s, t)$  is the sub-image of  $ks_{xy}$ .

### J. Image Subtraction

This stage performs the image reduction process using arithmetic operations. The value of each image pixel is reduced by the reducing image pixel value. The equation used in the reduction process is presented in Formula (13).

$$CO(x, y) = CI1(x, y) - CI2(x, y) \quad (13)$$

Where the variable symbol used is the same as equation (10). A process illustration of subtraction is presented in Fig. 8.

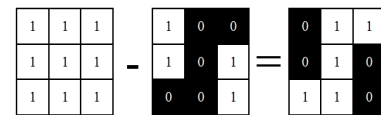


Fig. 8 Illustration of image subtraction process

### K. Region Properties

At this stage, the object labeling process is carried out using the region properties (regionprops) function. Regionprops is used to measure the set of properties of each labeled region in the label matrix [45]. Regionprops can only detect white objects, namely pixels with a value of 1 as the foreground, while black ones, which have a value of 0 as the background [46].

In the regionprops function, an object is assumed to be an ellipse so that each object has a major axis length and a minor axis length. The value farthest from the centroid to the outermost pixel is for the major axis length, while the closest distance is to get the minor axis length value [47]. The area representation using the ellipse approach is presented in Fig. 9 [48].



Fig. 9 Area representation using an ellipse shape approach

### III. RESULT AND DISCUSSION

In this study, only one test image was presented from 34 images of patients with COVID-19. This input image is 485 x 394-pixel size in JPG format. The patient identities contained in the image are hidden on display in the article to maintain the code of ethics. So that the image presented only includes the chest cavity as the outermost boundary, namely the image presented in Fig. 10.



Fig. 10 One of the input images for COVID-19 patients

The input image presented in Fig. 10 cannot be identified the objects contained in the thorax because the features of each object are not clearly prominent. To accentuate the features, an image contrast enhancement is done using the CLAHE algorithm. In the CLAHE process, decrease the pixel value with low intensity and increase the pixel value with high intensity. The results of this process are presented in Fig. 11, where a significant change has been made to the gray values of each pixel in the image so that objects can begin to be identified.



Fig. 11 The result of the image enhancement process

The next step is to convert the image from the CLAHE process into a binary image. This stage performs the conversion process using the thresholding Algorithm. The value of each pixel is converted to 1 (one) if it has a value equal to or higher than the threshold, and the others are converted to a value of 0 (zero). The results of this process are presented in Fig. 12, where there has been a separation of the object as foreground with the background. The result of this process is still noise in the image, which is scattered randomly and irregularly.

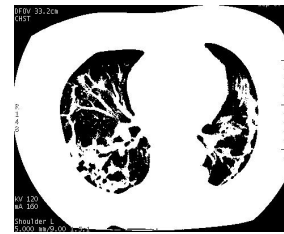


Fig. 12 The result of the conversion process to binary image

Furthermore, the morphological operation process is carried out on the binary image. Morphological operations were carried out twice with the Morphological Opening technique. The first morphological operation uses a 3 x 3 disk element (strel) structure. The result of this operation is to obtain an object identification image. This image is initialized with the Identify Image (OII) object.

The second morphological operation uses a 15 x 15 disk element (strel) structure. The result of this operation is to obtain the boundaries of the objects in the image. This image is initialized with a Boundary Object Image (BOI). The results of this process are presented in Fig. 13.

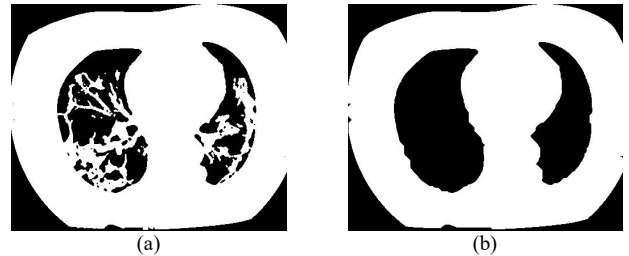


Fig. 13 The result of the morphological operation process (a) OII image, (b) BOI image

The resulting image is presented in Fig. 13 has eliminated noise in the image. After that, it is followed by an inverted process to the OII and BOI images. The value of each pixel from the image with a value of 1 is changed to 0, and the value of 0 is changed to 1. The image produced from this process is to emphasize the objects contained in the image even though there are other unwanted objects. The results of this process are presented in Fig. 14.

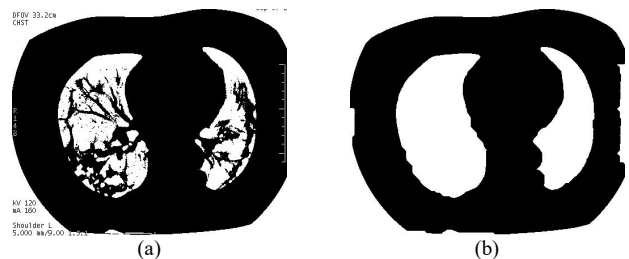


Fig. 14 Inverted process results (a) OII image, (b) BOI image

The next step is to process the Active Contour Model on the two inverted images. The process aims to segment objects in the image. The number of iterations performed on the image is 400 times for OII image and 800 times for the BOI image. The resulting image is in the form of an Area of Interest (AoI) from the thorax cavity only, so that the area outside the thorax is eliminated. The results of this process are presented in Fig. 15.

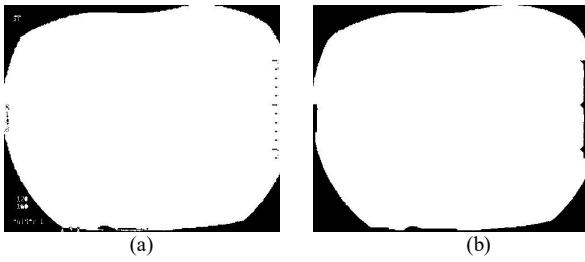


Fig. 15 Process results of the Active Contour Model (a) OII image, (b) BOI image

Furthermore, the process of adding the inverted image results with the active contour model image, namely the OII image in Fig. 14 (a) with Fig. 15 (a) and the BOI image in Fig. 14 (b) with Fig. 15 (b). The value of each pixel will change according to the operation 0 added by 0 to 0, 0 added by 1 to 1, 1 added by 0 to 1, and 1 added by 1 to 1. The results of this process are presented in Fig 16.

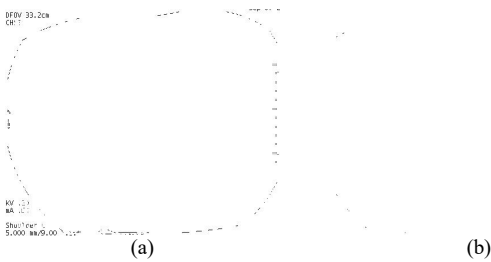


Fig. 16 Result of image addition process (a) OII image, (b) BOI image

The next step is to convert the two matrix values to a gray scale. This process aims to bring back the observed objects and eliminate other objects. The image generated from this process still has noise which is also randomly scattered and irregular. The results of this process are presented in Fig. 17.

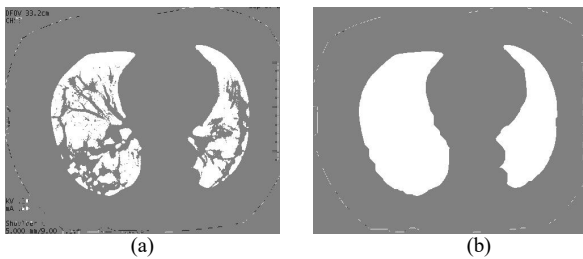


Fig. 17 Result of convert matrix to grayscale (a) OII image, (b) BOI image

Noise still exists in the image presented in Fig. 17 removed by the filtering process. The filter algorithm used is the Median Filter with a 5 x 5 filter. The results of this process are presented in Fig. 18.



Fig. 18 The result of filtering process (a) OII image, (b) BOI image

Then the two images are converted back to binary so that the objects identified are clearer and less noise. The results of this process are presented in Fig. 19.



Fig. 19 The result of the conversion process to binary (a) OII image, (b) BOI image

The next step is to reduce the conversion results to binary from the OII image with the BOI image. This process aims to further highlight the objects that will be identified in the image and eliminate other objects. Only the pixel value at a certain position is fixed, that is if the subtraction is 1. Thus, the resulting image can be identified every complete object with an edge. The results of this stage are presented in Fig. 20.

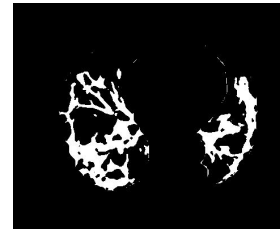


Fig. 20 Subtraction image

The final stage of this model is the process of identifying objects using the regionprops function and labeling each object. For each identified pixel, the pixel value changes to red. Changed pixel color is the object and the edge (edge detection) of these objects. These objects are identified as GGO. The results at this stage are presented in Fig. 21

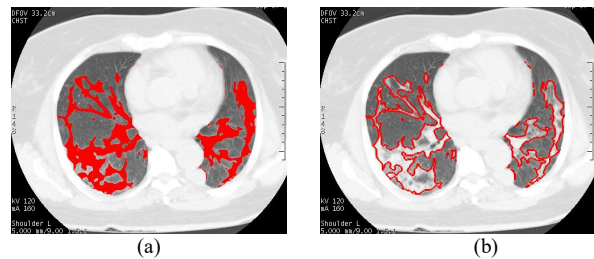


Fig. 21 GGO identification image (red color) (a) object (b) edge detection

Image shown in Fig. 21 show that the objects in the image have been identified very well, so that the pattern from GGO can be recognized. The next step is to count the number of pixels of objects in the image. The number of pixels to determine the thorax area is calculated in the image presented in Fig. 19 (b), while the area of GGO is calculated in Fig. 21 (a). From the results of this calculation, it can be determined the level of comparison of the area of GGO to the area of the thorax. The calculation used to determine the level of this ratio is the ratio equation presented in Formula 14.

$$\text{Ratio}\% = \frac{\text{GGO Area}}{\text{Thorax Area}} \times 100\% \quad (14)$$

Where the ratio is level of the GGO area to the thorax area multiplied by 100%. Based on the results of Formula 14, it can be concluded that the greater the value of the GGO area, the wider the area of the thorax containing GGO. The magnitude of this ratio indicates the higher the severity of patients suffering from Covid-19. The results of calculations for all patients are presented in Table 1.

TABLE I  
COMPARISON RATIO OF GGO WITH THORAX

Image Name	Area GGO (Pixel)	Area Thorax (Pixel)	Ratio (%)
Patient_01	14,970	43,650	34.2
Patient_02	6,693	28,568	23.4
Patient_03	2,963	34,935	8.4
Patient_04	6,632	46,776	14.1
Patient_05	4,057	18,410	22.0
Patient_06	2,801	36,473	7.6
Patient_07	4,274	41,522	10.2
Patient_08	4,774	47,118	10.1
Patient_09	2,662	25,417	10.4
Patient_10	3,179	44,254	7.1
Patient_11	2,595	40,317	6.4
Patient_12	2,798	40,805	6.8
Patient_13	8,463	38,377	22.0
Patient_14	5,767	34,337	16.7
Patient_15	3,659	47,366	7.7
Patient_16	2,004	40,980	4.8
Patient_17	1,217	24,571	4.9
Patient_18	4,934	32,979	14.9
Patient_19	5,156	38,136	13.5
Patient_20	4,231	30,777	13.7
Patient_21	2,332	41,141	5.6
Patient_22	1,221	30,902	3.9
Patient_23	4,000	26,712	14.9
Patient_24	6,907	43,518	15.8
Patient_25	4,921	47,171	10.4
Patient_26	5,209	55,429	9.3
Patient_27	5,513	41,194	13.3
Patient_28	1,849	41,200	4.4
Patient_29	7,411	48,321	15.3
Patient_30	8,258	48,393	17.0
Patient_31	1,930	40,987	4.7
Patient_32	1,570	27,557	5.6
Patient_33	7,888	24,077	32.7
Patient_34	2,203	26,357	8.3

The results of image processing presented in Table 1 state that every thorax of a COVID-19 patient has GGO. GGO will result in an increased weakening of the function of the thorax. The percentage ratio in this study was 3.9% for the smallest and 34.2% for the largest. The higher percentage value indicates the severity of patients with Covid-19, so these patients must receive more intensive treatment.

#### IV. CONCLUSION

From the results of CT-scan thorax image processing of COVID-19 sufferers, it is concluded that the GGO pattern can be identified very well. From the identification results, the area of GGO in pixels can be calculated, and the ratio between GGO and thorax area. The results of this ratio can help doctors make quick decisions in taking appropriate treatment actions.

#### REFERENCES

- [1] L. Chang, Y. Yan, and L. Wang, "Coronavirus Disease 2019: Coronaviruses and Blood Safety," *Transfusion Medicine Reviews*, vol. 34, no. 2, pp. 75-80, 2020. DOI: 10.1016/j.tmr.2020.02.003.
- [2] T. Singhal, "A Review of Coronavirus Disease-2019 (COVID-19)," *The Indian Journal of Pediatrics*, vol. 87, pp. 281-286, 2020. DOI: 10.1007/s12098-020-03263-6.
- [3] C.-C. Lai, T.-P. Shih, W.-C. Ko, H.-J. Tang, and P.-R. Hsueh, "Severe acute respiratory syndrome coronavirus 2 (SARS-CoV-2) and corona virus disease-2019 (COVID-19): the epidemic and the challenges," *International Journal of Antimicrobial Agents*, vol. 55, no. 3, 2020. DOI: 10.1016/j.ijantimicag.2020.105924.
- [4] F. A. Rabi, M. S. Al Zoubi, G. A. Kasasbeh, D. M. Salameh, and A. D. Al-Nasser, "SARS-CoV-2 and Coronavirus Disease 2019: What We Know So Far," *Pathogens*, vol.9, 2020. DOI: 10.3390/pathogens9030231.
- [5] Y. Han, and H. Yang, "The transmission and diagnosis of 2019 novel coronavirus infection disease (COVID-19): A Chinese perspective," *Journal of Medical Virology*, vol. 92, no. 6, pp. 639-644, 2020. DOI: 10.1002/jmv.25749.
- [6] D. Wang, B. Hu, C. Hu, et al., "Clinical Characteristics of 138 Hospitalized Patients With 2019 Novel Coronavirus-Infected Pneumonia in Wuhan, China," *Journal of the American Medical Association*, vol. 323, no. 11, pp. 1061-1069, 2020. DOI: 10.1001/jama.2020.1585.
- [7] S. Srivatsan, P. D. Han, K. van Raay, C. R. Wolf, et al., "Preliminary support for a dry swab, extraction free protocol for SARS-CoV-2 testing via RT-qPCR," *bioRxiv*, 2020. DOI: 10.1101/2020.04.22.056283.
- [8] S. Ahuja, B. K. Panigrahi, N. Dey, V. Rajinikanth, and T. K. Gandhi, "Deep transfer learning-based automated detection of COVID-19 from lung CT scan slices," *Applied Intelligence*, 2020. DOI: 10.1007/s10489-020-01826-w.
- [9] M. Chung, A. Bernheim, X. Mei, N. Zhang, M. Huang, X. Zeng, J. Cui, W. Xu, Y. Yang, Z. A. Fayad, A. Jacobi, K. Li, S. Li, and H. Shan, "CT Imaging Features of 2019 Novel Coronavirus (2019-nCoV)," *Radiology*, vol. 295, no. 1, pp. 202-207, 2020. DOI: 10.1148/radiol.2020200230.
- [10] A. M. Sirisha and P. Venkateswararao, "Image Processing Techniques on Radiological Images of Human Lungs Effected by COVID-19," *JOIV: International Journal on Informatics Visualization*, vol. 4, no. 2, pp. 69, 2020. DOI: 10.30630/joiv.4.2.359.
- [11] W. Guan, Z. Ni, Y. Hu, W. Liang, et al., "Clinical Characteristics of Coronavirus Disease 2019 in China," *The New England Journal of Medicine*, vol. 382, pp. 1708-1720, 2020. DOI: 10.1056/NEJMoa2002032.
- [12] W. Herring. "Learning radiology : recognizing the basics," 4th ed., Philadelphia: Elsevier. pp. 2-4, 2020.
- [13] S. Salehi, A. Abedi, S. Balakrishnan, and A. Gholamrezaezhad, "Coronavirus Disease 2019 (COVID-19): A Systematic Review of Imaging Findings in 919 Patients," *American Journal of Roentgenology*, vol. 215, no. 1, pp. 87-93, 2020. DOI: 10.2214/AJR.20.23034.
- [14] S. Zhou, Y. Wang, T. Zhu, and L. Xia, "CT Features of Coronavirus Disease 2019 (COVID-19) Pneumonia in 62 Patients in Wuhan, China," *American Journal of Roentgenology*, vol. 214, no. 6, pp. 1287-1294, 2020. DOI: 10.2214/AJR.20.22975.
- [15] W. Zhao, Z. Zhong, X. Xie, Q. Yu, and J. Liu, "Relation Between Chest CT Findings and Clinical Conditions of Coronavirus Disease (COVID-19) Pneumonia: A Multicenter Study," *American Journal of Roentgenology*, vol. 214, no. 5, pp. 1072-1077, 2020. DOI: 10.2214/AJR.20.22976.
- [16] V. Rajinikanth, N. Dey, A. N. J. Raj, A. E. Hassani, K. C. Santosh, and N. S. M. Raja, "Harmony-Search and Otsu based System for

- Coronavirus Disease (COVID-19) Detection using Lung CT Scan Images,” *arXiv*, 2020. arXiv: 2004.03431.
- [17] D. P. Fan, T. Zhou, G. P. Ji, Y. Zhou, G. Chen, H. Fu, J. Shen, and L. Shao, “Inf-Net: Automatic COVID-19 Lung Infection Segmentation from CT Images,” *arXiv*, 2020. arXiv:2004.14133.
- [18] D. Das, K. C. Santosh, and U. Pal, “Truncated inception net: COVID-19 outbreak screening using chest X-rays,” *Physical and Engineering Sciences in Medicine*, vol. 43, pp. 915–925, 2020. DOI: 10.1007/s13246-020-00888-x.
- [19] T. Ozturk, M. Talo, E. A. Yildirim, U. B. Baloglu, O. Yildirim, and U. R. Acharya, “Automated detection of COVID-19 cases using deep neural networks with X-ray images,” *Computers in Biology and Medicine*, vol. 121, 2020. DOI: 10.1016/j.compbiomed.2020.103792.
- [20] S. Minaee, R. Kafteh, M. Sonka, S. Yazdani, and G. J. Soufi, “Deep-COVID: Predicting COVID-19 from chest X-ray images using deep transfer learning,” *Medical Image Analysis*, vol. 65, 2020. DOI: 10.1016/j.media.2020.101794.
- [21] I. D. Apostolopoulos, and T. A. Mpesiana, “Covid-19: automatic detection from X-ray images utilizing transfer learning,” *Physical and Engineering Sciences in Medicine*, vol. 43, pp. 635-640, 2020. DOI: 10.1007/s13246-020-00865-4.
- [22] A. Narin, C. Kaya, and Z. Pamuk, “Automatic Detection of Coronavirus Disease (COVID-19) Using X-ray Images and Deep Convolutional Neural Networks,” *arXiv*, 2020. arXiv: 2003.10849.
- [23] G. Siracusano, A. L. Corte, M. Gaeta, G. Cicero, M. Chiappini, and G. Finocchio, “Pipeline for Advanced Contrast Enhancement (PACE) of chest X-ray in evaluating COVID-19 patients by combining bidimensional empirical mode decomposition and CLAHE,” *Sustainability*, vol. 12, 2020. DOI: 10.3390/su12208573.
- [24] M. Loey, G. Manogaran, and N. E. M. Khalifa, “A deep transfer learning model with classical data augmentation and CGAN to detect COVID-19 from chest CT radiography digital images,” *Neural Computing and Applications*, 2020. DOI: 10.1007/s00521-020-05437-x.
- [25] D. Singh, V. Kumar, Vaishali and M. Kaur, “Classification of COVID-19 patients from chest CT images using multi-objective differential evolution-based convolutional neural networks,” *European Journal of Clinical Microbiology & Infectious Diseases*, 2020. DOI: 10.1007/s10096-020-03901-z.
- [26] Y. Yunus, J. Harlan, J. Santony, R. Hidayat, and J. Naam, “Enhancement on Enlarge Image for Identification Lumbar Radiculopathy at Magnetic Resonance Imaging,” *TEM Journal*, vol. 9, no. 2, pp. 649-655, 2020. DOI: 10.18421/TEM92-30.
- [27] S. M. Pizer, E. P. Amburn, J. D. Austin, R. Cromartie, A. Geselowitz, et al., “Adaptive histogram equalization and its variations, Computer Vision, Graphics, and Image Processing,” *Computer Vision, Graphics and Image Processing*, vol. 39, pp. 355–68, 1987. DOI: 10.1016/S0734-189X(87)80186-X.
- [28] Sonali, S. Sahu, A. K. Singh, S. P. Ghrra, M. Elhoseny, “An approach for de-noising and contrast enhancement of retinal fundus image using CLAHE,” *Optics & Laser Technology*, vol. 110, pp. 87-98, 2019. DOI: 10.1016/j.optlastec.2018.06.061.
- [29] W. N. J. H. W. Yussof, M. S. Hitam, E. A. Awalludin, and Z. Bachok, “Performing contrast limited adaptive histogram equalization technique on combined color models for underwater image enhancement,” *International Journal of Interactive Digital Media*, vol. 1, no. 1, pp. 1-6, 2013.
- [30] D. J. Hemanth, O. Deperlioglu and U. Kose, “An enhanced diabetic retinopathy detection and classification approach using deep convolutional neural network,” *Neural Computing and Applications*, vol. 2, no. 3, pp. 707-721, 2020. DOI: 10.1007/s00521-018-03974-0.
- [31] P. Parida, and R. Rout, “Transition region based approach for skin lesion segmentation,” *ELCVIA: Electronic Letters on Computer Vision and Image Analysis*, vol. 19, no. 1, pp. 28-37, 2020. DOI: 10.5565/rev/elcvia.1177.
- [32] G. K. Chadha, A. Srivastava, A. Singh, R. Gupta, and D. Singla, “An Automated Method for Counting Red Blood Cells using Image Processing,” *Procedia Computer Science*, vol. 167, pp. 769-778, 2020. DOI: 10.1016/j.procs.2020.03.408.
- [33] E. Murali, and K. Meena, “Brain Tumor Detection from MRI using Adaptive Thresholding and Histogram based Techniques,” *Scalable Computing: Practice and Experience*, vol. 21, no. 1, pp. 3-10, 2020. DOI: 10.12694/scpe.v21i1.1600.
- [34] A. Ledda, “Mathematical Morphology in Image Processing,” Doctoral dissertation, PhD thesis, Ghent University, Ghent, Belgium, 2007.
- [35] R. M. Haralick, S. R. Sternberg, and X. Zhuang, “Image analysis using mathematical morphology,” *IEEE Transactions on Pattern Analysis and Machine Intelligence*, vol. 4, pp. 532-550, 1987. DOI: 10.1109/TPAMI.1987.4767941.
- [36] J. Serra, *Image Analysis and Mathematical Morphology*, London: Academic Press, 1982.
- [37] B. Li, and S. T. Acton, “Active contour external force using vector field convolution for image segmentation,” *IEEE Transactions on Image Processing*, vol. 16, no. 8, pp. 2096-2106, 2007. DOI: 10.1109/TIP.2007.899601.
- [38] R. Ronfard, “Region-based strategies for active contour models,” *International Journal of Computer Vision*, vol. 13, no. 2, pp. 229-251, 1994. DOI: 10.1007/BF01427153.
- [39] M. Kass, A. Witkin, and D. Terzopoulos, “Snakes: Active contour models,” *International Journal of Computer Vision*, vol. 1, no. 4, pp. 321-331, 1988. DOI: 10.1007/BF00133570.
- [40] R. C. Gonzalez, and R. E. Woods, *Digital image processing*, Upper Saddle River, New Jersey: Prentice Hall, 2002.
- [41] Y. Zhang, J. Qian, O. Zaltzhendler, et al., “Analysis of in vivo uterine peristalsis in the non-pregnant female mouse,” *Interface Focus*, vol. 9, no. 4, 2019. DOI: 10.1098/rsfs.2018.0082.
- [42] L. Novamizanti, A. L. Prasasti, and I. F. N. Kiranda, “Comparison of discrete cosine transform and dual-tree complex wavelet transform based on arithmetic coding in medical image compression,” In *Journal of Physics: Conference Series*, 2020, vol. 1367, no. 1, p. 012021. DOI: 10.1088/1742-6596/1367/1/012021.
- [43] Y. Zhu, and C. Huang, “An improved median filtering algorithm for image noise reduction,” *Physics Procedia*, vol. 25, pp. 609-616, 2012. DOI: 10.1016/j.phpro.2012.03.133.
- [44] M. P. Sukassini, and T. Velmurugan, “Noise removal using morphology and median filter methods in mammogram images,” In *The 3rd International Conference on Small and Medium Business*, 2016, pp. 413-419.
- [45] A. A. Sheikh, M. S. Azmi, M. A. Aziz, M. N. Al-Mhiqani, and S. S. Bafjaish, “Diacritic segmentation technique for arabic handwritten using region-based,” *Indonesian Journal of Electrical Engineering and Computer Science*, vol. 18, no. 1, pp. 478-484, 2020. DOI: 10.11591/ijeecs.v18.i1.pp478-484.
- [46] J. Ananthanarasimhan, P. Leelesh, M. S. Anand, and R. Lakshminarayana, “Validation of projected length of the rotating gliding arc plasma using ‘regionprops’ function,” *Plasma Research Express*, vol. 2, no. 3, 2020. DOI: 10.1088/2516-1067/abae49.
- [47] N. J. Shoumy, P. Ehkan, S. N. Yaakob, M. S. Ali, and S. Khatun, “Feature extraction for neural network pattern recognition for bloodstain analysis,” *International Journal of Applied Engineering Research*, vol. 11, no. 15, pp. 8583-8589, 2016.
- [48] F. S. Pranata, J. Naam, and R. Hidayat, “Color Feature Segmentation Image for Identification of Cotton Wool Spots on Diabetic Retinopathy Fundus,” *International Journal on Advanced Science, Engineering and Information Technology*, vol. 10, no. 3, pp. 974-979, 2020. DOI: 10.18517/ijaseit.10.3.11877.